Saturn's auroral morphology and field-aligned currents during a solar wind compression

S. V. Badman[a], G. Provan[b], E. J. Bunce[b], D. G. Mitchell[c], H. Melin[b,d], S. W. H. Cowley[b], A. Radioti[e], W. S. Kurth[f], W. R. Pryor[g], J. D. Nichols[b], S. L. Jinks[b], T. S. Stallard[b], R. H. Brown[h], K. H. Baines[i], M. K. Dougherty[j]

[a] *Department of Physics, Lancaster University, Bailrigg, Lancaster, LA1 4YB, UK*
[b] *Department of Physics and Astronomy, University of Leicester, University Road, Leicester, LE1 7RH, UK*
[c] *JHU APL, 111999 Johns Hopkins Road, Laurel, MD 20723, USA*
[d] *Space Environment Technologies, USA*
[e] *LPAP - Université de Liège, Sart Tilman - B5c, 17 Allé du 6 Aout, 4000 - LIEGE, Belgium*
[f] *Department of Physics and Astronomy, University of Iowa, 613 Van Allen Hall, Iowa City, IA 52242-1479, USA*
[g] *Central Arizona College, Coolidge, AZ 85128, USA*
[h] *LPL, University of Arizona, Tucson, AZ 85721, USA*
[i] *JPL, Pasadena, CA 91109, USA*
[j] *Imperial College London, London, SW7 2AZ, UK*

Abstract

On 21–22 April 2013, during a coordinated auroral observing campaign, instruments onboard Cassini and the Hubble Space Telescope observed Saturn's aurora while Cassini traversed Saturn's high latitude auroral field lines. Signatures of upward and downward field-aligned currents were detected ~~on the nightside~~ in the nightside magnetosphere in the magnetic field and plasma measurements. The location of the upward current corresponded to the bright ultraviolet auroral arc seen in the auroral images, and the downward current region was located poleward of the upward current in an aurorally dark region. Within the polar cap magnetic field and plasma fluctuations were identified with periods of ∼ 20 and ∼ 60 min. The northern

Email address: s.badman@lancaster.ac.uk (S. V. Badman)

and southern auroral ovals were observed to rock in latitude in phase with the respective northern and southern planetary period oscillations. A solar wind compression impacted Saturn's magnetosphere at the start of 22 April 2013, identified by an intensification and extension to lower frequencies of the Saturn kilometric radiation, with the following sequence of effects: (1) intensification of the auroral field-aligned currents; (2) appearance of a localised, intense bulge in the dawnside (04–06 LT) aurora while the midnight sector aurora remained fainter and narrow; (3) latitudinal broadening and poleward contraction of the nightside aurora, where the poleward motion in this sector is opposite to that expected from a model of the auroral oval's usual oscillation. These observations are interpreted as the response to tail reconnection events, initially involving Vasyliunas-type reconnection of closed mass-loaded magnetotail field lines, and then proceeding onto open lobe field lines, causing the contraction of the polar cap region on the ~~nightside~~night side.

Keywords: Saturn, magnetosphere, Aurorae

---

1. Introduction

Saturn's auroral intensity and morphology are known to respond strongly to the solar wind conditions that envelop the magnetosphere. The 'quiet' aurora is typically composed of a 1–2° wide arc, more intense on the ~~dawnside~~ dawn side than the dusk, and located at 14–16° co-latitude ~~on~~ in the southern dayside sector (Grodent et al., 2005; Badman et al., 2006; Lamy et al., 2009; Carbary, 2012). The northern aurora is typically located 1–2° closer to the pole than that in the south because of the higher magnetic field strength in the northern hemisphere (Dougherty et al., 2005; Nichols et al., 2009). However, the location and width of the aurora are very variable, and substructure of the oval is commonly seen (Badman et al., 2006, 2014b; Grodent et al., 2011; Meredith et al., 2013). Large-scale auroral intensifications have been observed in response to the arrival of solar wind shocks ahead of high pressure regions (Prangé et al., 2004; Clarke et al., 2005, 2009; Crary et al., 2005; Nichols et al., 2014). These intensifications have been interpreted as the signatures of compression-induced magnetotail reconnection (Cowley et al., 2005; Bunce et al., 2005b). Latitudinal broadening of the main auroral emissions and smaller-scale features have been related to intensifications of the ring current and to more localised injections in the magnetosphere (Mitchell et al., 2009a; Radioti et al., 2013b; Lamy et al., 2013). Small spot and arc features at and poleward of the main arcs of emission have been identified as the signatures of reconnection ~~on~~ in both the dayside and nightside magnetosphere (Gérard et al., 2005; Radioti et al., 2011, 2013a, 2014; Badman et al., 2012a, 2013; Jackman et al., 2013; Meredith et al., 2013, 2014). Measurements of field-aligned currents associated with the main auroral emission by Cassini have shown that the upward current carried by downward auroral electrons is co-located with the polar cap boundary on the ~~dayside~~ day side (Bunce et al., 2008a) and maps to the outer ring current or outer magnetosphere on the ~~nightside~~ night side (Talboys et al., 2011).

Many features of Saturn's magnetosphere demonstrate so-called 'planetary period oscillations' in their intensity and/or location, as reviewed, for example, by Carbary & Mitchell (2013). The planetary period perturbations in the magnetic field at high latitudes take the form of planet-centered transverse rotating dipoles in each hemisphere (Provan et al., 2009). The near-equatorial field perturbations take the form of quasi-uniform rotating fields aligned with the effective dipoles in the equatorial plane, combined with north-south fields, resulting in arched loops (Andrews et al., 2010). The effective dipoles rotate independently in the northern and southern hemispheres with periods close to 10.7 h. Field-aligned currents are associated with these magnetic field perturbations. The currents are directed across the pole at high-latitudes, i.e. field-aligned downward into the ionosphere on one side of the pole, field-aligned upward from the ionosphere on the other side of the pole, and partially closing in the equatorial plane of the outer magnetosphere.

The planetary period oscillations are also evident in both the location and intensity of Saturn's aurora. The centres of the auroral ovals have been observed to oscillate along an ellipse with a latitudinal amplitude of 1–2° (Nichols et al., 2008, 2010b). Nichols et al. (2010b) suggested that the northern auroral oval would be offset in the direction of the northern effective rotating dipole, and the southern oval offset in the direction opposite to the southern effective rotating dipole. However, more recent work has indicated that the maximum equatorward displacement of the southern auroral oval occurs 90° ahead in azimuth of the southern effective dipole direction, equivalent to 6 h later in LT (G. Hunt and S.W.H. Cowley, personal communication, 2014). Applying this to the northern hemisphere suggests that the northern auroral oval should exhibit its maximum equatorward displacement 90° behind the northern effective dipole direction, equivalent to 6 h earlier in LT. The northern and southern auroral ovals are then expected to rock around their central positions in phase with the rotation of the northern and southern effective transverse dipoles. The intensity of the aurora in each hemisphere is also shown to be modulated at the respective period according to the rotation of the field-aligned currents associated with the effective transverse dipoles, although a local time asymmetry also remains, as mentioned above (Sandel et al., 1982; Nichols et al., 2010a; Badman et al., 2012b; Lamy et al., 2013; Carbary, 2013).

Saturn's aurora are most commonly observed at ultraviolet and infrared wavelengths, corresponding to emission from H and H_2 in the UV and H_3^+ in the infrared. Badman et al. (2011) and Melin et al. (2011, 2014) have shown that the main auroral arcs are co-located at these wavelengths such that the UV and IR main emissions can be directly compared. However, there are differences at higher and lower latitudes reflecting the different response of these emitting species to auroral electron energy, thermospheric temperature, or emitting species lifetime (Tao et al., 2011; Badman et al., 2014a).

It is clear from the discussion above that Saturn's ~~aurora~~ aurorae respond to both external (solar wind) and internal (planetary rotation) dynamics. In this study the in situ and remote signatures of auroral precipitation are analysed over an interval from the 2013 coordinated observing campaign. This interval included observations of both the northern and southern aurorae and the response to a solar wind compression. These observations provide an opportunity to disentangle the planetary period rocking of the auroral oval from a localised poleward contraction in response to solar wind compression-driven magnetotail dynamics. In the sections below we first describe the field and particle measurements made by Cassini and then show the sequence of auroral observations. These observations are then related to each other, the rocking of the auroral oval identified, and the effects of the solar wind compression investigated.

2. In situ observations of fields and particles by Cassini

Figure 1 shows the observations made by Cassini on 2013-111 and 2013-112, around the periapsis of Rev 187 which occurred at the end of 2013-111. Cassini was moving from the southern pre-midnight sector to the northern post-midnight sector. The upper panel shows the electric field spectrogram detected by the Radio and Plasma Wave Science instrument (RPWS, Gurnett et al., 2004), with Saturn Kilometric Radiation (SKR) evident at 100s of kHz and broadband auroral hiss at up to $\sim$ 100 Hz. The magnetic field measured by the magnetometer (Dougherty et al., 2004) is plotted in spherical polar coordinates referenced to the planet's dipole ~~/spin axis~~axis (which is closely aligned with the spin axis) in the lower panel. The residual field components are plotted after subtraction of a model of the internal planetary magnetic field including dipole, quadrupole and octupole components (Burton et al., 2010).

At the start of the interval Cassini was traversing southern lobe field lines, indicated by the quiet magnetic field. The presence of auroral hiss in the electric field spectrogram in the upper panel is also associated with the high latitude magnetic field lines (Gurnett et al., 2010). The equatorial crossing from south to north is identified by the reversal of the B_r component of the field (green) from negative to positive.

Sharp changes in the azimuthal B_ϕ component of the magnetic field were also observed. As discussed in several previous studies, localised perturbations in B_ϕ are indicative of field-aligned currents, the upward portion of which is associated with the auroral emission (Bunce et al., 2008a; Talboys et al., 2009b,a, 2011; Badman et al., 2012a). The B_ϕ component can be used to derive the meridional ionospheric Pedersen current by application of Ampère's law to a current ring centered on the planet's dipole axis. This relationship is given by

$$I_P = \pm \frac{\rho B_\phi}{\mu_0}, \tag{1}$$

where I_P is the meridional ionospheric current per radian of azimuth, ρ is the cylindrical radial distance of Cassini from Saturn's dipole axis and the negative sign applies for the northern hemisphere and positive for the southern hemisphere (e.g. Bunce et al., 2008a; Talboys et al., 2011). This analysis also assumes that the structures are stationary relative to the moving spacecraft, which is a reasonable assumption in this case as the spacecraft was at small radial distance, 6–9 R_S, and moving relatively quickly across the field lines of interest. Assuming approximate axi-symmetry, increases and decreases in the meridional ionospheric current require downward and upward field-aligned currents to maintain current continuity.

The B_ϕ perturbations and deduced meridional ionospheric current are shown for the intervals when Cassini crossed the southern and northern nightside auroral current regions in Figure 2. Each of these shows a 12 h sub-interval of that in Figure 1, with the southern encounter on 2013-111 (~~a–c~~a–d) and the northern encounter on 2013-112 (~~d–g~~e–h). Figures 2~~b and~~

~~f~~ c and g show the meridional ionospheric Pedersen current, positive equatorward, in black (left hand axis). The ionospheric colatitude of the spacecraft is also shown in grey (right hand axis) where the mapping to the ionosphere was performed using the Burton et al. (2010) model of the planetary field plus a contribution from the ring current modelled by Bunce et al. (2008b). Figures 2c and g show the B_ϕ perturbations from which I_P was derived.

The large scale structure of the field-aligned currents identified during these intervals is as follows: the increase from $B_\phi \sim 0$ to $B_\phi > 0$ at 14 UT on 2013-111, as Cassini moved equatorward in the southern hemisphere, indicates a downward field-aligned current. This was followed by the opposite signature indicating an upward current at 18 UT. These downward and upward currents are indicated by the orange and purple shading, respectively, on Figure 2~~b~~c. The magnitude of the upward current was ~ 2.3 MA rad^{-1}. In the northern hemisphere on 2013-112 the strong reversal from $B_\phi > 0$ to $B_\phi < 0$ at 03:40 UT, while Cassini travelled poleward, indicates an upward current of magnitude ~ 5.1 MA rad^{-1}. This is indicated by the purple shading on Figure 2f. The upward current was followed by an overall decrease in the B_ϕ magnitude until 07 UT, indicative of downward current (orange shading on Figure 2f). ~~A full description of the large scale currents during the 2013 high latitude orbits is given by Jinks et al. (in preparation).~~

The signatures of the field-aligned currents in the plasma and wave observations are now examined. Figure 2a shows two notable spikes in the broadband wave power at 12:30 UT and 13:30 UT on 2013-111, extending to ~ 1 kHz. During these spikes the lower frequency, quasi-continuous emission disappeared, which could be a signature of Cassini passing through the edge of the resonance cone, where it can only detect the higher frequencies (Kopf, 2010). The second and more intense of the spikes followed a small, sharp increase in B_ϕ within the downward current region indicated by the orange shading on Figure 2~~b~~c, while the first spike was detected just outside the downward current region. The LEMMS sensor also detected an increased flux of electrons at energies of a few tens of keV during this interval from 2013-111 12:20–14:10 UT~~(data not shown)~~, shown in Figure 2b. These observations suggest narrow or transient enhancements of the downward current structure detected between 2013-111 13:00–14:40 UT (orange shading). This is consistent with the increased flux of energetic electrons - supposed to be travelling upward to the spacecraft. No similar spikes in the broadband wave power were observed during the upward current encounters indicated by the purple shading on Figures 2~~b and f~~ c and g at ∼17:30–18:00 UT on 2013-111 and 03:00–04:30 UT on 2013-112. The broadband waves (up to ∼ 100 Hz) seen in Figures 2a and ~~d~~ e were not detected in the regions equatorward of the upward current in either the northern or southern hemisphere, as shown by Gurnett et al. (2010).

During and after the encounter with the upward current region at 03:00–04:30 UT on 2013-112 all components of the magnetic field exhibited repeated small fluctuations until ∼ 12 UT (see the lower panel of Figure 1 and Figure 2~~g~~h). Two spikes in the broadband waves (up to ∼ 100 Hz) were detected by RPWS at ∼ 06 and 07 UT (Figure 2~~d~~e), similar to those observed at 12:30 and 13:30 UT on 2013-111 (shown in Figure 2a). Small fluctuations in B_ϕ towards lower values also occurred at these times, within the downward current region indicated by the orange shading on Figure 2~~f~~g. Figure 2~~e~~f shows energetic proton fluxes measured by the Ion Neutral Camera (INCA), part of the Magnetospheric Imaging Instrument (MIMI, Krimigis et al., 2004). ~~(The brief decrease in all proton fluxes at 10 UT on 2013-112 in Figure 2e corresponds to an instrument pointing change at the end of the auroral imaging interval.)~~ Peaks in the ~~55–227~~90–360 keV proton fluxes were also detected at 06 and 07 UT on 2013-112. These wave and plasma intensifications are commonly seen in Cassini observations and have been related to strong downward current regions, although the cause of the ~ 1 h periodicity is unknown (Mitchell et al., 2009b, 2014; Badman et al., 2012a; Roussos et al., 2014).

From approximately 07–12 UT on 2013-112 the field fluctuations ~~became~~ were of smaller magnitude (up to 1 nT) and more regular (Figure 2~~g~~h). During this interval smaller peaks in the proton fluxes (Figure 2~~e~~f) and broadband wave intensity (Figure 2~~d~~e) were also present. The period of these smaller fluctuations was approximately 20 min. At this time Cassini was moving ~~towards the dayside~~ sunward across the northern polar cap at high latitudes within the auroral oval.

The electric field spectra shown in Figure 1 and 2~~d~~ e show that the SKR intensified and extended to lower frequencies from ~ 5 UT on 2013-112. This is indicative of a solar wind compression of the magnetosphere (Kurth et al., 2005; Badman et al., 2008) and signifies an increased flux of field-aligned, accelerated electrons and an extension of the SKR source region to higher altitudes.

3. Auroral observations

Three instruments were used to make auroral observations during this interval. Infrared auroral emission from the molecular ion H_3^+ was detected by the Cassini Visual and Infrared Mapping Spectrometer (VIMS, Brown et al., 2004). VIMS acquires a full wavelength spectrum (0.85–5.1 µm) at each pixel position in its field of view (FOV) sequentially, where 1 pixel = 0.5×0.5 mrad and the maximum FOV is 64×64 pixels. The total time required to build up a 2-D pseudo-image was 72 min for the observations used in this study. The data were projected onto a $0.25° \times 0.25°$ planetocentric polar grid using the peak emission height of 1100 km above the 1 bar reference spheroid (Stallard et al., 2012). The emission intensities used here were determined from multiple wavelength bins containing H_3^+ emission lines around 3.5 µm.

The UV aurorae were observed by the Cassini Ultraviolet Imaging Spectrometer (UVIS, Esposito et al., 2004) and the Hubble Space Telescope (HST) Advanced Camera for Surveys (ACS). The UVIS observations were acquired by scanning the slit (1.5×64 mrad) across the auroral region, observing the wavelength range 115.5–191.2 nm. Pseudo-images were constructed by combining three slit scans covering different portions of the auroral region using the method described by Grodent et al. (2011). Each pseudo-image composed of three scans took about 80 min to build up. These images were polar projected onto a $0.1° \times 0.1°$ planetocentric polar grid using the peak emission height for H_2 emission of 1100 km above the 1 bar reference spheroid (Gérard et al., 2009).

Turning to the HST observations, the Solar Blind Channel (SBC) of ACS has a FOV of 35×31 arcsec^2 and an average plate scale of ~ 0.032 arcsec pixel^{-1}. The image processing pipeline is described in detail by Clarke et al. (2009). The images used in this study were taken using the F115LP long-pass filter which includes emission from H Lyman-α and H_2 Lyman and Werner bands in the range 115–170 nm. The exposure time was 15 min for each image. These were also polar projected onto a $0.1^\circ \times 0.1^\circ$ planetocentric polar grid using the peak emission height of 1100 km above the 1 bar reference spheroid. Note that as each instrument covers a different wavelength range we do not compare intensities in this study but instead interpret the shape and location of the emission in each case.

The sequence of observations of Saturn's aurora during this interval is shown in Figures 3 and 4. Figure 3a is a pseudo-image of the southern infrared aurora taken by Cassini VIMS, where the view is looking down through the planet to the southern pole with dawn to the left and dusk to the right. The remaining images are of the northern aurora taken by HST/ACS (3b, 3c, and 4d), UVIS (4a and b) and VIMS (4c), looking down on the northern pole with local noon at the bottom, dawn to the left and dusk to the right. The yellow grid indicates latitudes at 10° intervals. The white line indicates the trajectory of Cassini mapped to the appropriate hemisphere using the Burton et al. (2010) model of Saturn's magnetic field and a model ring current from Bunce et al. (2008b). The white labelled circles indicate the start of days 111–113, and the yellow square indicates the magnetic footprint of Cassini along this path at the central time of the image in each panel (the times labelled in the upper right corner of each panel). The orange and purple shaded portions of the trajectory indicate the regions of downward and upward field aligned current, respectively, identified from the magnetic field data. For the images taken on 2013-111 and shown in Figure 3 these are the southern hemisphere current regions identified on 2013-111 in Figure 2~~b~~c. For the images taken on 2013-112 and shown in Figure 4 they are the northern hemisphere current regions identified on 2013-112 in Figure 2~~f~~g. The dashed yellow arrow shows the direction in which the auroral oval is expected to be tilted at that time, where in the southern hemisphere (Figure 3a), this is 90° ahead in azimuth of the southern effective rotating transverse dipole, and in the northern hemisphere it is 90° behind the northern effective rotating transverse dipole (G. Hunt and S.W.H. Cowley, personal communication, 2014). The azimuthal directions of the effective dipoles are taken from the empirical model by Provan et al. (2014).

The VIMS observations in Figure 3a at 09:14 UT on 2013-111 show a very narrow auroral arc, $< 1°$ latitude wide, with a discontinuity at local midnight. The intense patches at the pre-midnight edge of the instrument field of view are contamination from scattered light and ~~does~~ do not represent auroral emission. ~~These observations~~ The discontinuity in the auroral arc was observed to rotate to later LT over the three VIMS images taken on this day (of which the first is shown here) and may be related to a flow discontinuity or superposition of the rotating field-aligned currents. The sequence of VIMS observations and the possible causes of the discontinuity are described in more detail by Melin et al. (2014). A few hours later HST observed the northern UV aurora, shown in Figures 3b and c. Although the midnight region conjugate to that observed in the south by VIMS was not visible because of the viewing geometry, the aurorae at other local times remained narrow, especially around dawn.

Figure 4a and b show observations of the northern ultraviolet aurorae made by Cassini UVIS during scans centered on 2013-112 03:32 and 05:06 UT. In the first of these observations the aurorae formed a relatively narrow arc (1–2° latitude) of variable intensity extending from pre-midnight through dawn to pre-noon. In the second observation the arc had moved to slightly higher latitude and contained an intense bulge at 04–06 LT extending $\sim$ 1° poleward of the centre of the arc. ~~The variability in the shape of the auroral emission during this sequence is being analysed by Radioti et al. (in preparation).~~

Figure 4c shows two consecutive observations of the northern infrared aurora made by Cassini VIMS, centred on times of 2013-112 06:27 UT and 07:41 UT. The auroral arcs remained narrow and of variable intensity along the midnight region but became relatively wider ($\sim$ 3° latitude) and more intense in the pre-dawn region captured in the later image at 2013-112 07:41 UT. (The patch of intense emission in the bottom left corner of the FOV at 2013-112 07:41 UT is again non-auroral contamination present at all wavelengths, while the arc identified at higher latitudes is auroral emission.) As these two images are separated by 1 h

Finally, Figure 4d shows an HST observation of the northern UV aurora at 2013-112 08:45 UT. The midnight region was not observed because of the viewing angle, but the post-midnight auroral arc was at higher latitude and broader ($\sim$ 4° latitude) than in previous observations. The most intense region was post-dawn.

4. Correspondence between in situ and auroral observations

Comparison of Cassini's mapped trajectory and the southern auroral image shown in Figure 3a with the corresponding electric field spectra and magnetic field measurements shown in Figure 2~~a–c~~ a–d shows that the spacecraft was on polar cap field lines poleward of the auroral oval (observed in the infrared) until after 12 UT on 2013-111. The downward current signature was identified in the MAG data at 2013-111 14 UT while Cassini was on field lines mapping to 15° co-latitude in the southern ionosphere or $\sim$ 14° co-latitude in the northern ionosphere. Figure 3c shows an image of the northern aurora at the start of Cassini's encounter with the downward current region at 13:36 UT on 2013-111. The sub-spacecraft portion of the aurora was not visible at this time, but extrapolation between the pre- and post-midnight arcs of the aurora that were observed suggests that the downward current region was located just poleward of the nightside auroral arc. The upward current was encountered four hours later, when Cassini's position mapped to 19° in the southern hemisphere or 17° in the northern hemisphere. This suggests that the auroral current system and main emission had moved a few degrees equatorward in the time between the last auroral image (Figure 3c) and the in situ detection of the upward current, since it is the downward electrons carrying the upward current that are expected to generate the main auroral arc.

The next feature of interest is the strong upward field-aligned current detected by Cassini at 2013-112 03:40 UT as it moved to higher latitudes over the northern nightside region. This was detected during the UVIS scan interval used to build image Figure 4a. At this location the field line mapped to $\sim 17°$ co-latitude in the northern hemisphere as indicated on Figure 4a, which is at the poleward edge of the observed auroral arc. The full duration of the encounter with the upward current signature was 03:05–04:25 UT on 2013-112, during which time Cassini moved 1.5° poleward in the ionosphere. This corresponds to the width of the auroral arc observed by UVIS: $\sim 1°$ in this region, combined with the $\sim 1°$ poleward motion of the aurora arc which occurred between the two scans of this region shown in Figures 4a and b, therefore confirming the relationship, previously identified on the ~~nightside~~ night side by Bunce et al. (2014), between the upward current signature and the aurora.

As described in Section 2 above, the subsequent interval from 04–12 UT on 2013-112 was characterised by perturbations in the magnetic field, wave electric field, and proton fluxes and encompasses the region identified as a downward field-aligned current by the orange shading on Figure 2~~f~~g. Throughout this interval Cassini was poleward of the aurora and moving sunward across the dark northern polar cap towards higher latitudes~~and the dayside~~, as shown in Figures 4b–d. At 12 UT on 2013-112 Cassini reached a location of 06 LT, 9° colatitude, and 7.6 R_S radial distance, from which point the signatures were no longer obvious in the magnetic field data and the measured auroral hiss became less intense. It is yet to be determined whether this decrease in the observed signals is due to rotation of the downward current region associated with the auroral hiss out of the range of detection by the spacecraft, or a change in spacecraft LT, latitude, or altitude. The cause of the periodicity in the downward current region is as yet unknown, and these observations show that, while the previously-known 1 h periodicity is detected for short intervals ~~/~~or restricted spatial regions in the southern and northern polar caps poleward of the upward current at the polar cap boundary, bursts occurring with a shorter period of approximately 20 mins are also detected at higher latitudes. These shorter period bursts were detected for long intervals, across a large spatial region and from a range of spacecraft altitudes. Their origin is being explored in an ongoing study.

5. Oscillation and contraction of the auroral oval

The locations of Saturn's auroral ovals have been observed to oscillate by 1–2° in latitude in phase with the planetary period magnetic field perturbations (Nichols et al., 2008, 2010b). As described in the Introduction, the azimuth along which the centre of the northern oval is expected to be offset ~~in the direction 90° behind in azimuth (6 h earlier in LT) the direction~~ lags the azimuth of the northern effective transverse rotating dipole ~~, and the~~ by 90°, while the azimuth along which the centre of the southern oval is expected to be offset ~~in the direction 90° ahead~~ leads the azimuth of the southern effective dipole ~~direction~~by 90°. The effective dipoles rotate at the respective northern and southern rotation periods, such that the auroral ovals rock about their central position over the same periods.

The oscillations of the auroral oval are evident in the sequence of two HST images of the northern UV aurorae taken on 2013-111. In Figure 3b and c, the direction in which the oval is expected to be tilted is indicated by the yellow dashed arrow at the central time of each image. These arrows are reproduced in Figure 5, colour-coded according to the time of the image, as labelled in the top left corner. The location of the peak auroral emission on each image is also shown by the solid coloured lines. A circle was fitted to these points for each image and the circle centres are marked by the coloured crosses. The difference in azimuth of the northern effective dipole direction between these two images was $\sim 50°$ and the expected tilt of the auroral oval and its centre changes from being directed towards 18 LT to about 21:30 LT. The lines showing the location of the peak auroral emission at both dawn and dusk, and the crosses marking the fitted circle centres follow this predicted motion: tilting away from dusk at the time of the second image. The radii of the fitted circles remained similar at 15.2° and 14.8° for the two images, confirming that this is a tilting of the oval, not an expansion.

The description in Section 4 of the correspondence between the field aligned currents and the auroral emission on 2013-111 also revealed that the upward field-aligned current was detected in the southern hemisphere mapping to a location $\sim 1 - 2°$ equatorward of where the nightside aurora was observed 4 h earlier (Figure 3c). At the time that the upward current was detected, 18 UT on 2013-111, the southern auroral oval was expected to be tilted towards midnight, such that it would appear at its lowest latitudes in this sector. This ~~explains why the upward current could be detected~~ is consistent with the detection of the upward current at lower latitudes than where the aurora were observed earlier in the day, and provides further evidence for the regular rocking of both the southern and northern auroral ovals on 2013-111.

The same analysis has been applied to the UVIS, VIMS, and HST images acquired on 2013-112 (Figures 4a–d), with results shown in Figure 6, covering approximately half a planetary period oscillation. The northern auroral oval was expected to be tilted towards dawn during the first image, then shift towards noon and finally duskward. The auroral oval was predicted to be most tilted towards noon during the image at 2013-112 06:27 UT (green line) such that the nightside part of the auroral oval should be located at its highest latitudes at this time. The cyan, yellow, and red lines showing the peak intensity of the observed aurorae in the later images were displaced duskward of that in the first image, as expected. The auroral emissions shown in Figures 4c and d cannot be fitted by a circle because of the limited FOV of the VIMS observations, and the poleward broadening of the aurora in the post midnight region and poleward shift of the pre-noon arc in the final HST image. Therefore fitted circle centres are not shown for these images.

At the time of the last image, the northern auroral oval was expected to be displaced duskward and anti-sunward compared to the previous two images (green and yellow lines). The red line on Figure 6 shows that the oval had indeed shifted duskward compared to the earlier images (blue, cyan, yellow lines), however, the region closest to midnight had moved to higher latitudes instead of lower latitudes. Figure 4d shows that this contraction to higher latitudes is due to a combination of poleward broadening and motion of the post-midnight aurora as mentioned above. It is also apparent that the UV aurorae observed at 08:45 UT (Figure 4d) were generally thicker in latitude at most dawnside LT than in previous images. These observations clearly demonstrate that the change in location of the auroral oval during the latter part of the imaging interval was partly caused by a poleward contraction of the nightside aurorae, rather than purely the rocking of the auroral oval.

6. Significance of solar wind compression

Compression of the magnetosphere by the solar wind was inferred from the intensification and low frequency extension of the SKR emission early on 2013-112. The sequence of auroral observations taken on this day suggests that the aurora moved poleward by as much as $\sim 5^\circ$ latitude in the pre-dawn sector, over the 6 h between images Figure 4a and d. Only 1–2° of this motion is expected to be related to the regular oscillation of the oval. Furthermore the poleward contraction in the northern post-midnight region between the images at 06:27 and 08:45 UT on 2013-112 is opposite to the tilting of the auroral oval expected here. These observations therefore reveal a contraction of the auroral oval in this sector. Sections of the dawnside oval were also observed to broaden in latitude and brighten relative to noon and midnight sections, which indicates increased electron precipitation in these regions.

In previous studies, solar wind compressions have been linked to broad and intense auroral displays across the dawnside polar region (Prangé et al., 2004; Clarke et al., 2005; Nichols et al., 2014), and exceptionally high latitude encounters with auroral field-aligned currents (Bunce et al., 2010). Features within and at the equatorward boundary of the main emission have also been related to the injection of plasma and dipolarisation of magnetic field in the magnetotail (Bunce et al., 2005b; Mitchell et al., 2009a; Jackman et al., 2013).

In the sequence of observations analysed here, a localised poleward bulge of the auroral emission was first observed in the pre-dawn region after 04:20 on 2013-112, ~~which~~ and then appeared to move sunward (Figures 4b and c). At this time the midnight arcs remained narrow. This was followed by a poleward broadening of the post-midnight aurora and contraction of the polar cap ~~on the nightside~~ in this nightside region (Figure 4d). The SKR was intense throughout these observations and a low frequency extension was detected around 06 UT on 2013-112 (Figure 2~~d~~e).

The nightside upward and downward field-aligned currents were detected by Cassini in both hemispheres. The different duration of the field-aligned current encounters can be attributed to the relative motion of Cassini and the tilting auroral oval as described by Bunce et al. (2014). The upward current encounter in the southern hemisphere at $\sim$ 18 UT on 2013-111 was short as Cassini moved equatorward while this section of the southern auroral oval moved poleward as the oval tilted towards noon (see Figures 2~~b~~ c and 5). The northern hemisphere upward current encounter lasted longer because Cassini was moving poleward while this region of the northern auroral oval was also moving poleward - as the oval again tilted towards noon (see Figures 2~~f~~ g and 6).

The in situ measurements of the field-aligned currents show that the upward current measured in the northern hemisphere, 5.1 MA rad^{-1}, was more than twice as strong as that in the southern hemisphere on the previous day, 2.3 MA rad^{-1}. On average the nightside field-aligned currents have been shown to be of equal magnitude in both hemispheres (Talboys et al., 2011). Therefore we attribute the strengthening of the current measured in the northern hemisphere on 2013-112 to dynamics associated with the solar wind compression. Specifically, increased field-aligned current and electron precipitation in this region have been ~~theorised~~ predicted and observed as a result of tail reconnection, which sets up a pair of upward and downward field-aligned currents linking the ionosphere with the newly-dipolarised magnetic field in the magnetotail (Cowley et al., 2005; Bunce et al., 2010; Jackman et al., 2013; Nichols et al., 2014).

The observations are consistent with an interval of tail reconnection occurring for several hours. The bulge in the pre-dawn auroral oval was observed during the second UVIS observing interval (Figure 4b), indicating that it appeared after 04:20 UT. As noted above, the magnitude of the upward field-aligned current and the SKR emission associated with the upward current (downward auroral electrons) were enhanced at this time (Figure 2~~d and f~~e and g). Jackman et al. (2009) have related the occurrence of enhanced and low frequency SKR to reconnection events occurring in Saturn's magnetotail. The auroral bulge was observed within the main emission on the dawn sector, a region which maps to the outer ring current or outer magnetosphere (Belenkaya et al., 2014). The bulge is consistent with the injection of hot plasma into the dawnside outer magnetosphere following tail reconnection. However, other causes for the variability in the main oval structure have not been ruled out (Radioti et al., in preparation). Only the trailing edge of the bulge was visible in the next observation of this region at 07:41 UT (Figure 4c).

When the next VIMS image of the midnight region was taken, at 2013-112 06:27 UT, the location of the peak emission, shown in Figure 6, had shifted slightly poleward, but the image itself (Figure 4c) shows that a second, fainter but more continuous arc was still present at 17° co-latitude - the same as in the previous UVIS observation (Figure 4b). It is therefore not clear whether a poleward shift of the emission at midnight occurred between these observations. However, by the time of the final image, the shape of the aurora and the location of the peak emission shown in Figures 4d and 6 strongly suggest a poleward contraction of the oval in the post-midnight region. This is a signature of the closure of open magnetic flux from the magnetotail lobes (Cowley et al., 2005; Badman et al., 2005, 2014b; Nichols et al., 2014).

Compression of the magnetosphere by a high pressure region of the solar wind has been postulated to instigate reconnection in Saturn's magnetotail, as has been observed at the Earth (Boudouridis et al., 2003; Cowley et al., 2005). In this scenario, reconnection begins on the radially-stretched, mass-loaded, closed field lines which contain the tail current sheet. This leads to the disconnection of a plasmoid and dipolarisation of the planetward magnetic field lines - the tail part of the Vasyliunas cycle. These two effects (loss of mass via the disconnected plasmoid and planetward contraction of the connected field lines) then allow reconnection to proceed onto lobe field lines, closing open magnetic flux in the lobes as part of the Dungey cycle. The distinction and relationship between these processes has been described theoretically (e.g. Cowley et al., 2005), and detected in simulations (e.g. Jia et al., 2012) and observations (e.g. Jackman et al., 2011; Thomsen, 2013; Nichols et al., 2014).

We apply this sequence of events to describe the observations made during the current interval of study. On 2013-111 the aurorae were narrow, particularly on the ~~nightside~~night side, and demonstrated the regular planetary period rocking of the oval location (Figure 3). Early on 2013-112 a compression of the magnetosphere occurred, initially causing reconnection of closed, mass-loaded field lines in the central magnetotail. Plasma was injected into the outer ring current as the newly reconnected field lines contracted towards the planet and enhanced precipitation from this region resulted in intensified SKR (Figure 2de) and a bulge in the pre-dawn auroral oval (Figure 4b), visible at 05 UT. At this time and over the next couple of hours, the auroral oval near midnight remained narrow (Figure 4c). Reconnection then proceeded onto the open magnetotail lobe field lines, resulting in contraction of newly-closed field lines towards the planet. Field-aligned currents were set up in this region associated with the equatorward flow of the plasma at the ionospheric footprint of these field lines, across the open-closed field line boundary. At 08:45 UT the auroral signature of this process was detected as the post-midnight auroral arc became relatively more intense, broadened in latitude, and contracted towards the pole (Figure 4d).

Finally we note that dayside magnetic reconnection is also expected to be stronger under solar wind compression conditions (Jackman et al., 2004; Badman et al., 2005, 2013), and would occur in the noon sector. A possible auroral signature of dayside reconnection may be identified in the HST image taken at the end of the observing interval (Figure 4d). The intensification and poleward shift of the aurora in this sector are consistent with emission expected in the vicinity of the open-closed field line boundary during dayside reconnection, although it is not certain whether this is a signature of low latitude reconnection resulting in the opening of magnetic flux, or reconnection with lobe field lines which would not change the amount of open flux (Bunce et al., 2005a; Gérard et al., 2005; Meredith et al., 2014). The lack of this feature earlier in the observing sequence illustrates that the tail reconnection and enhanced nightside currents are not triggered by reconnection at the dayside magnetopause, as has been observed in the terrestrial magnetosphere (e.g. Anderson et al., 2014). Instead, tail reconnection can occur independently, although both processes are expected to be enhanced in solar wind compression regions.

7. Summary

We have examined the in situ and remote observations of Saturn's aurora in both the northern and southern hemispheres over a two-day interval during the 2013 coordinated auroral campaign. Signatures of auroral field-aligned currents were identified in the magnetic field. The downward current regions were also identified by characteristic ion and auroral hiss intensifications.

On 2013-111 the auroral arcs observed in both hemispheres were narrow and the auroral ovals rocked in latitude in phase with the planetary period oscillations. Early on 2013-112 a solar wind compression arrived, as identified by an intensification and extension to lower frequencies of the SKR. At this time a bulge appeared along the pre-dawn auroral oval, which appeared to have moved ~~towards the dayside~~ sunward when this region was next observed. The midnight sector aurora remained a narrow arc at this time. Subsequently, the post-midnight aurora broadened in latitude and contracted towards the pole. The motion in this sector was in the opposite direction to that expected from the planetary period oscillation.

In the interval when the auroral imaging and current measurement were simultaneous in the northern hemisphere, the upward current corresponded to the bright nightside auroral arc and the downward current mapped to the aurorally dark region poleward of this. The upward field-aligned current associated with the northern main oval was more than twice as strong as its southern hemisphere counterpart measured on the previous day (5.1 MA rad^{-1} compared to 2.3 MA rad^{-1}).

These observations are interpreted as the auroral response to tail reconnection instigated by solar wind compression of the magnetotail. The SKR intensification and auroral bulge are attributed to the injection of plasma into the outer ring current by reconnection on closed, mass-loaded tail field lines. The contraction of the reconnected field lines towards the planet then allowed reconnection to proceed onto lobe field lines, closing the open flux, and resulting in a contraction of the auroral oval in the post-midnight sector.

Acknowledgments This work uses observations with the NASA/ESA Hubble Space Telescope obtained at the Space Telescope Science Institute (STScI), which is operated by AURA, inc. for NASA. SVB was supported by a Royal Astronomical Society Research Fellowship. EJB, GP, HM, SWHC and TSS were supported by STFC grant ST/K001000/1, and EJB by a Philip Leverhulme Award. SLJ was supported by an STFC PhD studentship and JDN by an STFC Advanced Fellowship (ST/1004084/1). DGM was supported by the NASA Office of Space Science under Task Order 003 of contract NAS5-97271 between NASA Goddard Space flight Center and the Johns Hopkins University. The research at the University of Iowa was supported by NASA through contract 1415150 with the Jet Propulsion Laboratory.

References

Anderson, B. J., Korth, H., Waters, C. L., Green, D. L., Merkin, V. G., Barnes, R. J., & Dyrud, L. P. (2014). Development of large-scale Birkeland currents determined from the Active Magnetosphere and Planetary Electrodynamics Response Experiment. *Geophys. Res. Lett.*, *41*. doi:10.1002/2014GL059941.

Andrews, D. J., Coates, A. J., Cowley, S. W. H., Dougherty, M. K., Lamy, L., Provan, G., & Zarka, P. (2010). Magnetospheric period oscillations at Saturn: Comparison of equatorial and high-latitude magnetic field periods with north and south Saturn kilometric radiation periods. *J. Geophys. Res.*, *115*, 12252. doi:10.1029/2010JA015666.

Badman, S. V., Achilleos, N., Arridge, C. S., Baines, K. H., Brown, R. H., Bunce, E. J., Coates, A. J., Cowley, S. W. H., Dougherty, M. K., Fujimoto, M., Hospodarsky, G., Kasahara, S., Kimura, T., Melin, H., Mitchell, D. G., Stallard, T., & Tao, C. (2012a). Cassini observations of ion and electron beams at Saturn and their relationship to infrared auroral arcs. *J. Geophys. Res.*, *117*. doi:10.1029/2011JA017222.

Badman, S. V., Achilleos, N., Baines, K. H., Brown, R. H., Bunce, E. J., Dougherty, M. K., Melin, H., Nichols, J. D., & Stallard, T. (2011). Location of Saturn's northern infrared aurora determined from Cassini VIMS images. *Geophys. Res. Lett.*, *38*. doi:10.1029/2010GL046193.

Badman, S. V., Andrews, D. J., Cowley, S. W. H., Lamy, L., Provan, G., Tao, C., Kasahara, S., Kimura, T., Fujimoto, M., Melin, H., Stallard, T., Brown, R. H., & Baines, K. H. (2012b). Rotational modulation and local time dependence of Saturn's infrared H_3^+ auroral intensity. *J. Geophys. Res.*, *117*, A09228.

Badman, S. V., Branduardi-Raymont, G., Galand, M., Hess, S. L. G., Krupp, N., Lamy, L., Melin, H., & Tao, C. (2014a). Auroral Processes at the Giant Planets: Energy Deposition, Emission Mechanisms, Morphology and Spectra. *Space Sci. Rev.*, *180*. doi:10.1007/s11214-014-0042-x.

Badman, S. V., Bunce, E. J., Clarke, J. T., Cowley, S. W. H., Gérard, J.-C., Grodent, D., & Milan, S. E. (2005). Open flux estimates in Saturn's magnetosphere during the January 2004 Cassini-HST campaign, and implications for reconnection rates. *J. Geophys. Res.*, *110*. doi:10.1029/2005JA011240.

Badman, S. V., Cowley, S. W. H., Gérard, J.-C., & Grodent, D. (2006). A statistical analysis of the location and width of Saturn's southern auroras. *Ann. Geophys.*, *24*, 3533–3545.

Badman, S. V., Cowley, S. W. H., Lamy, L., Cecconi, B., & Zarka, P. (2008). Relationship between solar wind corotating interaction regions and the phasing and intensity of Saturn kilometric radiation bursts. *Ann. Geophys.*, *26*, 3641–3651.

Badman, S. V., Jackman, C. M., Nichols, J. D., & Gérard, J.-C. (2014b). Open flux in Saturn's magnetosphere. *Icarus*, *231*, 137–145. doi:10.1016/j.icarus.2013.12.004.

Badman, S. V., Masters, A., Hasegawa, H., Fujimoto, M., Radioti, A., Grodent, D., Sergis, N., Dougherty, M. K., & Coates, A. J. (2013). Bursty magnetic reconnection at Saturn's magnetopause. *Geophys. Res. Lett.*, *40*, 1027–1031. doi:10.1002/grl.50199.

Belenkaya, E. S., Cowley, S. W. H., Meredith, C. J., Nichols, J. D., Kalegaev, V. V., Alexeev, I. I., Barinov, O. G., Barinova, W. O., & Blokhina, M. S. (2014). Magnetospheric magnetic field modelling for the 2011 and 2012 HST Saturn aurora campaigns - implications for auroral source regions. *Ann. Geophys.*, *32*, 689–704.

Boudouridis, A., Zesta, E., Lyons, R., Anderson, P. C., & Lummerzheim, D. (2003). Effect of solar wind pressure pulses on the size and strength of the auroral oval. *J. Geophys. Res.*, *108*, 8012. doi:10.1029/2002JA009373.

Brown, R. H., Baines, K. H., Bellucci, G., Bibring, J. P., Buratti, B. J., Capaccioni, F., Cerroni, P., Clark, R. N., Coradini, A., Cruikshank, D., Drossart, P., Formisano, V., Jaumann, R., Langevin, Y., Matson, D. L., McCord, T. B., Mennella, V., Miller, E., Nelson, R. M., Nicholson, P. D., Sicardy, B., & Sotin, C. (2004). The Cassini Visual and Infrared Mapping Spectrometer (VIMS) investigation. *Space Sci. Rev.*, *115*, 111–168. doi:10.1007/s11214-004-1453-x.

Bunce, E. J., Arridge, C. S., Clarke, J. T., Coates, A. J., Cowley, S. W. H., Dougherty, M. K., Gérard, J.-C., Grodent, D., Hansen, K. C., Nichols, J. D., Southwood, D. J., & Talboys, D. L. (2008a). Origin of Saturn's aurora: Simultaneous observations by Cassini and the Hubble Space Telescope. *J. Geophys. Res.*, *113*. doi:10.1029/2008JA013257.

Bunce, E. J., Arridge, C. S., Cowley, S. W. H., & Dougherty, M. K. (2008b). Magnetic field structure of Saturn's dayside magnetosphere and its mapping to the ionosphere: Results from ring current modeling. *J. Geophys. Res.*, *113*. doi:10.1029/2007JA012538.

Bunce, E. J., Cowley, S. W. H., & Milan, S. E. (2005a). Interplanetary magnetic field control of Saturn's polar cusp aurora. *Ann. Geophys.*, *23*, 1405–1431. doi:10.5194/angeo-23-1405-2005.

Bunce, E. J., Cowley, S. W. H., Talboys, D. L., Dougherty, M. K., Lamy, L., Kurth, W. S., Schippers, P., Cecconi, B., Zarka, P., Arridge, C. S., & Coates, A. J. (2010). Extraordinary field-aligned current signatures in Saturn's high-latitude magnetosphere: Analysis of Cassini data during Revolution 89. *J. Geophys. Res.*, *115*, 10238. doi:10.1029/2010JA015612.

Bunce, E. J., Cowley, S. W. H., Wright, D. M., Coates, A. J., Dougherty, M. K., Krupp, N., Kurth, W. S., & Rymer, A. M. (2005b). In situ observations of a solar wind compression-induced hot plasma injection in Saturn's tail. *Geophys. Res. Lett.*, *322*, L20S04. doi:10.1029/2005GL022888.

Bunce, E. J., Grodent, D. C., Jinks, S. L., Andrews, D. J., Badman, S. V., Cowley, S. W. H., Dougherty, M. K., Kurth, W. S., Mitchell, D. G., Coates, A. J., & Provan, G. (2014). Cassini nightside observations of the oscillatory motion of Saturn's northern auroral oval. *J. Geophys. Res.*, *119*, 3528–3543. doi:10.1002/2013JA019527.

Burton, M. E., Dougherty, M. K., & Russell, C. T. (2010). Saturn's internal planetary magnetic field. *Geophys. Res. Lett.*, *37*. doi:10.1029/2010GL045148.

Carbary, J. F. (2012). The morphology of Saturn's ultraviolet aurora. *J. Geophys. Res.*, *117*. doi:10.1029/2012JA017670.

Carbary, J. F. (2013). Longitude dependences of Saturn's ultraviolet aurora. *Geophys. Res. Lett.*, *40*, 1902–1906. doi:10.1002/grl.50430.

Carbary, J. F., & Mitchell, D. G. (2013). Periodicities in Saturn's magnetosphere. *Rev. Geophys.*, *51*, 1–30. doi:10.1002/rog.20006.

Clarke, J. T., Gérard, J.-C., Grodent, D., Wannawichian, S., Gustin, J., Connerney, J., Crary, F., Dougherty, M., Kurth, W., Cowley, S. W. H., Bunce, E. J., Hill, T., & Kim, J. (2005). Morphological differences between Saturn's ultraviolet aurorae and those of Earth and Jupiter. *Nature*, *433*, 717–719. doi:10.1038/nature03331.

Clarke, J. T., Nichols, J., Gerard, J. C., Grodent, D., Hansen, K. C., Kurth, W., Gladstone, G. R., Duval, J., Wannawichian, S., Bunce, E., Cowley, S. W. H., Crary, F., Dougherty, M., Lamy, L., Mitchell, D., Pryor, W., Retherford, K., Stallard, T., Zieger, B., Zarka, P., & Cecconi, B. (2009). Response of Jupiter's and Saturn's auroral activity to the solar wind. *J. Geophys. Res.*, *114*. doi:10.1029/2008JA013694.

Cowley, S. W. H., Badman, S. V., Bunce, E. J., Clarke, J. T., Gérard, J.-C., Grodent, D., Jackman, C. M., Milan, S. E., & Yeoman, T. K. (2005). Reconnection in a rotation-dominated magnetosphere and its relation to Saturn's auroral dynamics. *J. Geophys. Res.*, *110*. doi:10.1029/2004JA010796.

Crary, F., Clarke, J., Dougherty, M., Hanlon, P., Hansen, K., Steinberg, J., Barraclough, B., Coates, A., Gerard, J., Grodent, D., Kurth, W., Mitchell, D., Rymer, A., & Young, D. (2005). Solar wind dynamic pressure and electric field as the main factors controlling Saturn's aurorae. *Nature*, *433*, 720–722. doi:DOI 10.1038/nature03333.

Dougherty, M. K., Achilleos, N., André, N., Arridge, C. S., Balogh, A., Bertucci, C., Burton, M. E., Cowley, S. W. H., Erdos, G., Giampieri, G., Glassmeier, K. H., Khurana, K. K., Leisner, J., Neubauer, F. M., Russell, C. T., Smith, E. J., Southwood, D. J., & Tsurutani, B. T. (2005). Cassini magnetometer observations during Saturn orbit insertion. *Science*, *307*, 1266–1270. doi:10.1126/science.1106098.

Dougherty, M. K., Kellock, S., Southwood, D. J., Balogh, A., Smith, E. J., Tsurutani, B. T., Gerlach, B., Glassmeier, K.-H., Gleim, F., Russell, C. T., Erdos, G., Neubauer, F. M., & Cowley, S. W. H. (2004). The Cassini Magnetic Field Investigation. *Space Sci. Rev.*, *114*, 331–383. doi:10.1007/s11214-004-1432-2.

Esposito, L. W., Barth, C. A., Colwell, J. E., Lawrence, G. M., McClintock, W. E., Stewart, A. I. F., Keller, H. U., Korth, A., Lauche, H., Festou, M. C., Lane, A. L., Hansen, C. J., Maki, J. N., West, R. A., Jahn, H., Reulke, R., Warlich, K., Shemansky, D. E., & Yung, Y. L. (2004). The Cassini Ultraviolet Imaging Spectrograph Investigation. *Space Sci. Rev.*, *115*, 299–361. doi:10.1007/s11214-004-1455-8.

Gérard, J.-C., Bonfond, B., Gustin, J., Grodent, D., Clarke, J. T., Bisikalo, D., & Shematovich, V. (2009). Altitude of Saturn's aurora and its implications for the characteristic energy of precipitated electrons. *Geophys. Res. Lett.*, *36*. doi:10.1029/2008GL036554.

Gérard, J.-C., Bunce, E. J., Grodent, D., Cowley, S. W. H., Clarke, J. T., & Badman, S. V. (2005). Signature of Saturn's auroral cusp: Simultaneous Hubble Space Telescope FUV observations and upstream solar wind monitoring. *J. Geophys. Res.*, *110*. doi:10.1029/2005JA011094.

Grodent, D., Gérard, J.-C., Cowley, S. W. H., Bunce, E. J., & Clarke, J. T. (2005). Variable morphology of Saturn's southern ultraviolet aurora. *J. Geophys. Res.*, *110*. doi:10.1029/2004JA010983.

Grodent, D., Gustin, J., Gérard, J.-C., Radioti, A., Bonfond, B., & Pryor, W. R. (2011). Small-scale structures in Saturn's ultraviolet aurora. *J. Geophys. Res.*, *116*. doi:10.1029/2011JA016818.

Gurnett, D. A., Kurth, W. S., Kirchner, D. L., Hospodarsky, G. B., Averkamp, T. F., Zarka, P., Lecacheux, A., Manning, R., Roux, A., Canu, P., Cornilleau-Wehrlin, N., Galopeau, P., Meyer, A., Boström, R., Gustafsson, G., Wahlund, J.-E., Åhlen, L., Rucker, H. O., Ladreiter, H. P., Macher, W., Woolliscroft, L. J. C., Alleyne, H., Kaiser, M. L., Desch, M. D., Farrell, W. M., Harvey, C. C., Louarn, P., Kellogg, P. J., Goetz, K., & Pedersen, A. (2004). The Cassini Radio and Plasma Wave Investigation. *Space Sci. Rev.*, *114*, 395–463. doi:10.1007/s11214-004-1434-0.

Gurnett, D. A., Persoon, A. M., Kopf, A. J., Kurth, W. S., Morooka, M. W., Wahlund, J.-E., Khurana, K. K., Dougherty, M. K., Mitchell, D. G., Krimigis, S. M., & Krupp, N. (2010). A plasmapause-like density boundary at high latitudes in Saturn's magnetosphere. *Geophys. Res. Lett.*, *37*, 16806. doi:10.1029/2010GL044466.

Jackman, C. M., Achilleos, N., Bunce, E. J., Cowley, S. W. H., Dougherty, M. K., Jones, G. H., Milan, S. E., & Smith, E. J. (2004). Interplanetary magnetic field at ∼9 AU during the declining phase of the solar cycle and its implications for Saturn's magnetospheric dynamics. *J. Geophys. Res.*, *109*. doi:10.1029/2004JA010614.

Jackman, C. M., Achilleos, N., Cowley, S. W. H., Bunce, E. J., Radioti, A., Grodent, D., Badman, S. V., Dougherty, M. K., & Pryor, W. (2013). Auroral counterpart of magnetic field dipolarizations in Saturn's tail. *Planet. Space. Sci.*, *82*, 34–42.

Jackman, C. M., Lamy, L., Freeman, M. P., Zarka, P., Cecconi, B., Kurth, W. S., Cowley, S. W. H., & Dougherty, M. K. (2009). On the character and distribution of lower-frequency radio emissions at Saturn and their relationship to substorm-like events. *J. Geophys. Res.*, *114*, 8211. doi:10.1029/2008JA013997.

Jackman, C. M., Slavin, J. A., & Cowley, S. W. H. (2011). Cassini observations of plasmoid structure and dynamics: Implications for the role of magnetic reconnection in magnetospheric circulation at Saturn. *J. Geophys. Res.*, *116*. doi:10.1029/2011JA016682.

Jia, X., Hansen, K. C., Gombosi, T. I., Kivelson, M. G., Tóth, G., DeZeeuw,

D. L., & Ridley, A. J. (2012). Magnetospheric configuration and dynamics of Saturn's magnetosphere: A global MHD simulation. *J. Geophys. Res.*, *117*. doi:10.1029/2012JA017575.

Kopf, A. J. (2010). *A multi-instrument study of auroral hiss at Saturn*. Ph.D. thesis University of Iowa.

Krimigis, S. M., Mitchell, D. G., Hamilton, D. C., Livi, S., Dandouras, J., Jaskulek, S., Armstrong, T. P., Boldt, J. D., Cheng, A. F., Gloeckler, G., Hayes, J. R., Hsieh, K. C., Ip, W.-H., Keath, E. P., Kirsch, E., Krupp, N., Lanzerotti, L. J., Lundgren, R., Mauk, B. H., McEntire, R. W., Roelof, E. C., Schlemm, C. E., Tossman, B. E., Wilken, B., & Williams, D. J. (2004). Magnetosphere Imaging Instrument (MIMI) on the Cassini Mission to Saturn/Titan. *Space Sci. Rev.*, *114*, 233–329. doi:10.1007/s11214-004-1410-8.

Kurth, W. S., Gurnett, D. A., Clarke, J. T., Zarka, P., Desch, M. D., Kaiser, M. L., Cecconi, B., Lecacheux, A., Farrell, W. M., Galopeau, P., Gérard, J.-C., Grodent, D., Prangé, R., Dougherty, M. K., & Crary, F. J. (2005). An Earth-like correspondence between Saturn's auroral features and radio emission. *Nature*, *433*, 722–725. doi:10.1038/nature03334.

Lamy, L., Cecconi, B., Prangé, R., Zarka, P., Nichols, J. D., & Clarke, J. T. (2009). An auroral oval at the footprint of Saturn's kilometric radio sources, colocated with the UV aurorae. *J. Geophys. Res.*, *114*, A10212. doi:10.1029/2009JA014401.

Lamy, L., Prangé, R., Pryor, W., Gustin, J., Badman, S. V., Melin, H., Stallard, T., Mitchell, D. G., & Brandt, P. C. (2013). Multi-spectral simultaneous diagnosis of Saturn's aurorae throughout a planetary rotation. *J. Geophys. Res.*, *118*, 1–27. doi:10.1002/jgra.50404.

Melin, H., Badman, S. V., Stallard, T. S., Dyudina, U., Nichols, J., O'Donoghue, J., Pryor, W. R., Baines, K. H., Miller, S., Gustin, J., Radioti, A., Tao, C., Meredith, C. J., & Blake, J. S. D. (2014). Simultaneous multi-scale and multi-instrument observations of Saturn's aurorae during the 2013 Observing Campaign. *Icarus*, *submitted*.

Melin, H., Stallard, T., Miller, S., Gustin, J., M., G., Badman, S. V., Pryor, W. R., O'Donoghue, J., Brown, R. H., & Baines, K. H. (2011). Simultaneous Cassini VIMS and UVIS observations of Saturn's southern aurora: comparing emissions from H, H_2 and H_3^+ at a high spatial resolution. *Geophys. Res. Lett.*, *38*. doi:10.1029/2011GL048457.

Meredith, C. J., Alexeev, I. I., Badman, S. V., Belenkaya, E. S., Cowley, S. W. H., Dougherty, M. K., Kalegaev, V. V., Lewis, G. R., & Nichols, J. D. (2014). Saturn's dayside UV auroras: Evidence for morphological dependence on the direction of the upstream interplanetary magnetic field. *J. Geophys. Res.*, *119*. doi:10.1002/2013JA019598.

Meredith, C. J., Cowley, S. W. H., Hansen, K. C., Nichols, J. D., & Yeoman, T. K. (2013). Simultaneous conjugate observations of small-scale structures in Saturn's dayside ultraviolet auroras – implications for physical origins. *J. Geophys. Res.*, *118*, 2244–2266. doi:10.1002/jgra.50270.

Mitchell, D. G., Carbary, J. F., Bunce, E. J., Radioti, A., Badman, S. V., Pryor, W. R., Hospodarsky, G. B., & Kurth, W. S. (2014). Recurrent Pulsations in Saturn's High Latitude Magnetosphere. *Icarus*, *submitted*.

Mitchell, D. G., Krimigis, S. M., Paranicas, C., Brandt, P. C., Carbary, J. F., Roelof, E. C., Kurth, W. S., Gurnett, D. A., Clarke, J. T., Nichols, J. D., Gérard, J.-C., Grodent, D. C., Dougherty, M. K., & Pryor, W. R. (2009a). Recurrent energization of plasma in the midnight-to-dawn quadrant of Saturn's magnetosphere, and its relationship to auroral UV and radio emissions. *Planet. Space. Sci.*, *57*, 1732–1742. doi:10.1016/j.pss.2009.04.002.

Mitchell, D. G., Kurth, W. S., Hospodarsky, G. B., Krupp, N., Saur, J., Mauk, B. H., Carbary, J. F., Krimigis, S. M., Dougherty, M. K., & Hamilton, D. C. (2009b). Ion conics and electron beams associated with auroral processes on Saturn. *J. Geophys. Res.*, *114*, A02212. doi:10.1029/2008JA013621.

Nichols, J. D., Badman, S. V., Baines, K. H., Brown, R. H., Bunce, E. J., Clarke, J. T., Cowley, S. W. H., Crary, F. J., Gérard, J.-C., Grocott, A., Grodent, D., Kurth, W. S., Melin, H., Mitchell, D. G., Pryor, W. R., & Stallard, T. S. (2014). Dynamic auroral storms on Saturn as observed by the Hubble Space Telescope. *Geophys. Res. Lett.*, *41*, 3323–3330. doi:10.1002/2014GL060186.

Nichols, J. D., Cecconi, B., Clarke, J. T., Cowley, S. W. H., Gérard, J.-C., Grocott, A., Grodent, D., Lamy, L., & Zarka, P. (2010a). Variation of Saturn's UV aurora with SKR phase. *Geophys. Res. Lett.*, *37*. doi:10.1029/2010GL044057.

Nichols, J. D., Clarke, J. T., Cowley, S. W. H., Duval, J., Farmer, A. J., Gérard, J.-C., Grodent, D., & Wannawichian, S. (2008). Oscillation of Saturn's southern auroral oval. *J. Geophys. Res.*, *113*. doi:10.1029/2008JA013444.

Nichols, J. D., Clarke, J. T., Gérard, J. C., Grodent, D., & Hansen, K. C. (2009). Variation of different components of Jupiter's auroral emission. *J. Geophys. Res.*, *114*, 6210. doi:10.1029/2009JA014051.

Nichols, J. D., Cowley, S. W. H., & Lamy, L. (2010b). Dawn-dusk oscillation of Saturn's conjugate auroral ovals. *Geophys. Res. Lett.*, *372*, L24102. doi:10.1029/2010GL045818.

Prangé, R., Pallier, L., Hansen, K. C., Howard, R., Vourlidas, A., Courtin, R., & Parkinson, C. (2004). An interplanetary shock traced by planetary auroral storms from the Sun to Saturn. *Nature*, *432*, 78–81. doi:10.1038/nature02986.

Provan, G., Andrews, D. J., Arridge, C. S., Coates, A. J., Cowley, S. W. H., Milan, S. E., Dougherty, M. K., & Wright, D. M. (2009). Polarization and phase of planetary-period magnetic field oscillations on high-latitude field lines in Saturn's magnetosphere. *J. Geophys. Res.*, *114*, 2225. doi:10.1029/2008JA013782.

Provan, G., Lamy, L., Cowley, S. W. H., & Dougherty, M. K. (2014). Planetary period oscillations in Saturn's magnetosphere: Comparison of magnetic oscillations and SKR modulations in the post-equinox interval. *J. Geophys. Res.*, *in press*. doi:10.1002/2014JA020011.

Radioti, A., Grodent, D., Gérard, J.-C., Bonfond, B., Gustin, J., Pryor, W., Jasinski, J. M., & Arridge, C. S. (2013a). Auroral signatures of multiple magnetopause reconnection at Saturn. *Geophys. Res. Lett.*, *40*, 4498–4502. doi:10.1002/grl.50889.

Radioti, A., Grodent, D., Gérard, J.-C., Bonfond, B., Pryor, W., Gustin, J., Mitchell, D., & Jackman, C. M. (2014). A remarkable magnetotail reconnection event at Saturn as observed by UVIS/Cassini. *Icarus*, *submitted*.

Radioti, A., Grodent, D., Gérard, J.-C., Milan, S. E., Bonfond, B., Gustin, J., & Pryor, W. R. (2011). Bifurcations of the main auroral ring at Saturn: ionospheric signatures of consecutive reconnection events at the magnetopause. *J. Geophys. Res.*, *116*. doi:10.1029/2011JA016661.

Radioti, A., Roussos, E., Grodent, D., Gérard, J.-C., Krupp, N., Mitchell, D. G., Gustin, J., Bonfond, B., & Pryor, W. (2013b). Signatures of magnetospheric injections in Saturn's aurora. *J. Geophys. Res.*, *118*, 1922–1933. doi:10.1002/jgra.50161.

Roussos, E., Krupp, N., Mitchell, D. G., Paranicas, C., Krimigis, S. M., Andriopoulou, M., Kurth, W. S., Masters, A., & Dougherty, M. K. (2014). Quasi-periodic injections of relativistic electrons in Saturn's outer magnetosphere. *Icarus*, *submitted*.

Sandel, B. R., Shemansky, D. E., Broadfoot, A. L., Holberg, J. B., Smith, G. R., McConnell, J. C., Strobel, D. F., Atreya, S. K., Donahue, T. M., Moos, H. W., Hunten, D. M., Pomphrey, R. B., & Linick, S. (1982). Extreme ultraviolet observations from the Voyager 2 encounter with Saturn. *Science*, *215*, 548–553. doi:10.1126/science.215.4532.548.

Stallard, T. S., Melin, H., Miller, S., Badman, S. V., Brown, R. H., & Baines, K. H. (2012). Peak emission altitude of Saturn's H_3^+ aurora. *Geophys. Res. Lett.*, *39*. doi:10.1029/2012GL052806.

Talboys, D. L., Arridge, C. S., Bunce, E. J., Coates, A. J., Cowley, S. W. H., & Dougherty, M. K. (2009a). Characterization of auroral current systems in Saturn's magnetosphere: High-latitude Cassini observations. *J. Geophys. Res.*, *114*. doi:10.1029/2008JA013846.

Talboys, D. L., Arridge, C. S., Bunce, E. J., Coates, A. J., Cowley, S. W. H., Dougherty, M. K., & Khurana, K. K. (2009b). Signatures of field-aligned currents in Saturn's nightside magnetosphere. *Geophys. Res. Lett.*, *36*. doi:10.1029/2009GL039867.

Talboys, D. L., Bunce, E. J., Cowley, S. W. H., Arridge, C. S., Coates, A. J., & Dougherty, M. K. (2011). Statistical characteristics of field-aligned currents in Saturn's nightside magnetosphere. *J. Geophys. Res.*, *116*. doi:10.1029/2010JA016102.

Tao, C., Badman, S. V., & Fujimoto, M. (2011). UV and IR auroral emission model for the outer planets: Jupiter and Saturn comparison. *Icarus*, *213*, 581–592. doi:10.1016/j.icarus.2011.04.001.

Thomsen, M. F. (2013). Saturn's magnetospheric dynamics. *Geophys. Res. Lett.*, *40*, 5337–5344. doi:10.1002/2013GL057967.

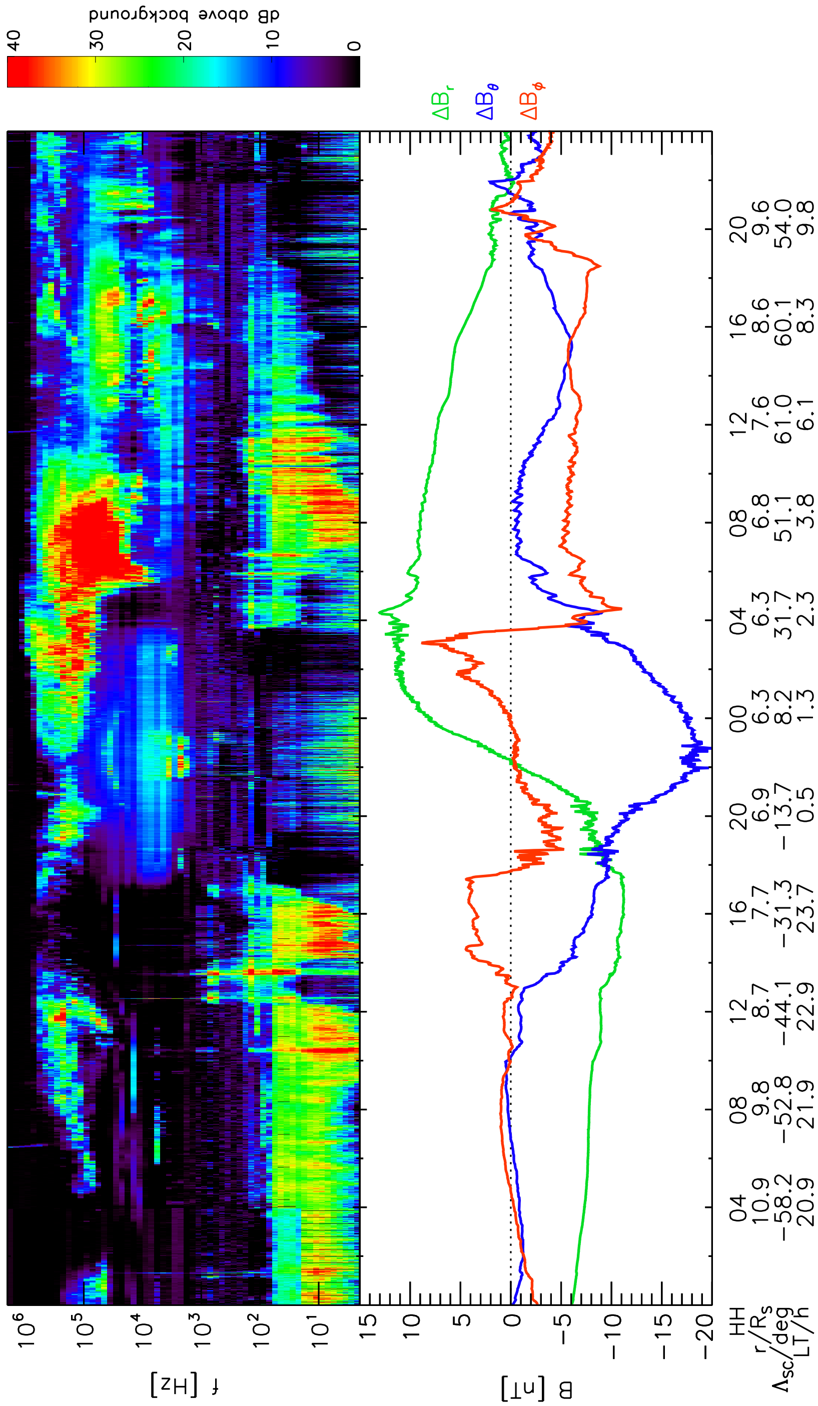

Figure 1: Field and plasma measurements made by Cassini during 2013-111 and 2013-112 (21 and 22 April). The top panel shows the wave frequency-time spectrogram measured by Cassini/RPWS. The bottom panel shows the residual components of the magnetic field in spherical polar coordinates. Cassini ephemeris data are also labelled on the x-axis, where r is the radial distance of the spacecraft from Saturn's centre, Λ_{SC} is the sub-spacecraft latitude, and LT is the local time.

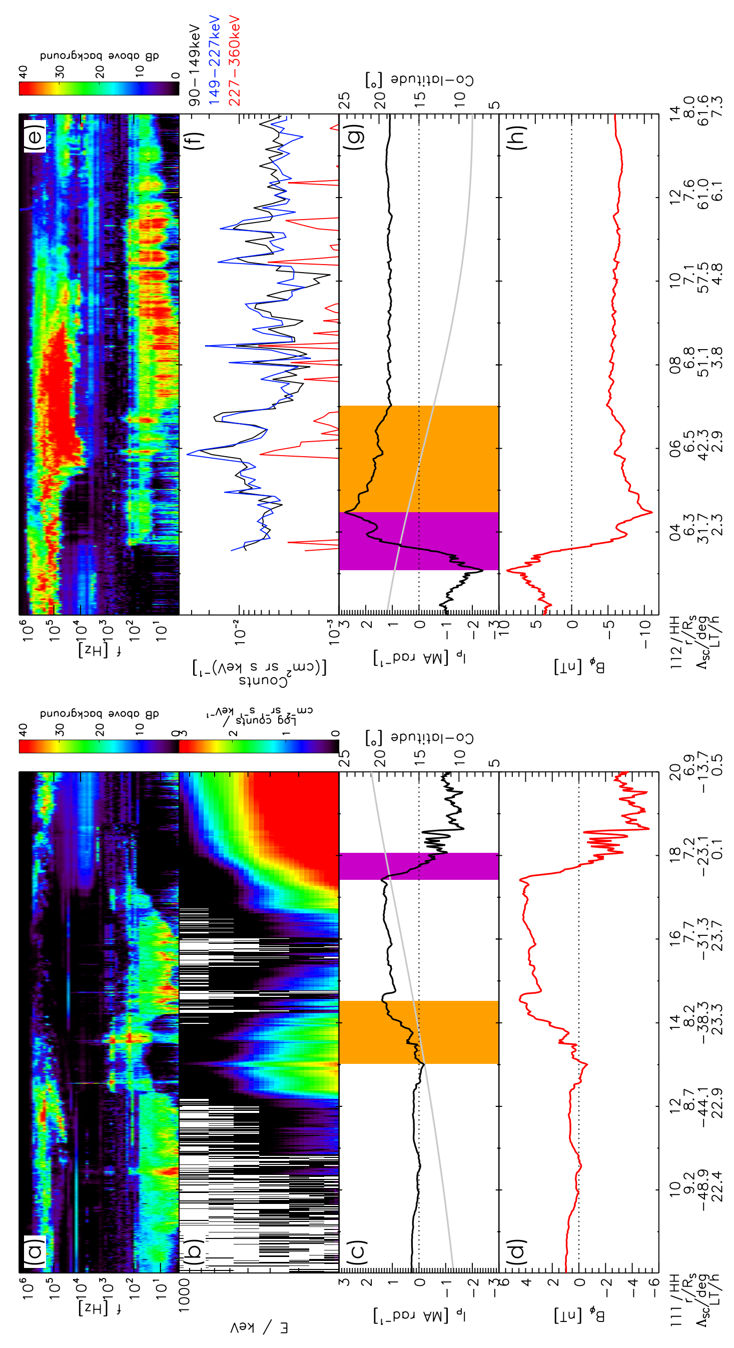

Figure 2: Auroral field-aligned currents measured by Cassini on 2013-111 08–20 UT and 2013-112 02–14 UT. (a) and (de) show the frequency-time spectrograms of waves measured by Cassini/RPWS. (b) fluxes of 200 keV–1 MeV electrons detected by LEMMS. (c) and (f) show the ionospheric colatitude of the spacecraft using a magnetic field model to map along the field line (grey line, right hand axis), and the meridional ionospheric Pedersen current per radian, positive equatorward (black line, left hand axis). (ed) and (g) show the B_ϕ component of the magnetic field. (e) shows the energetic proton counts at different energies 90–360 keV detected by INCA.

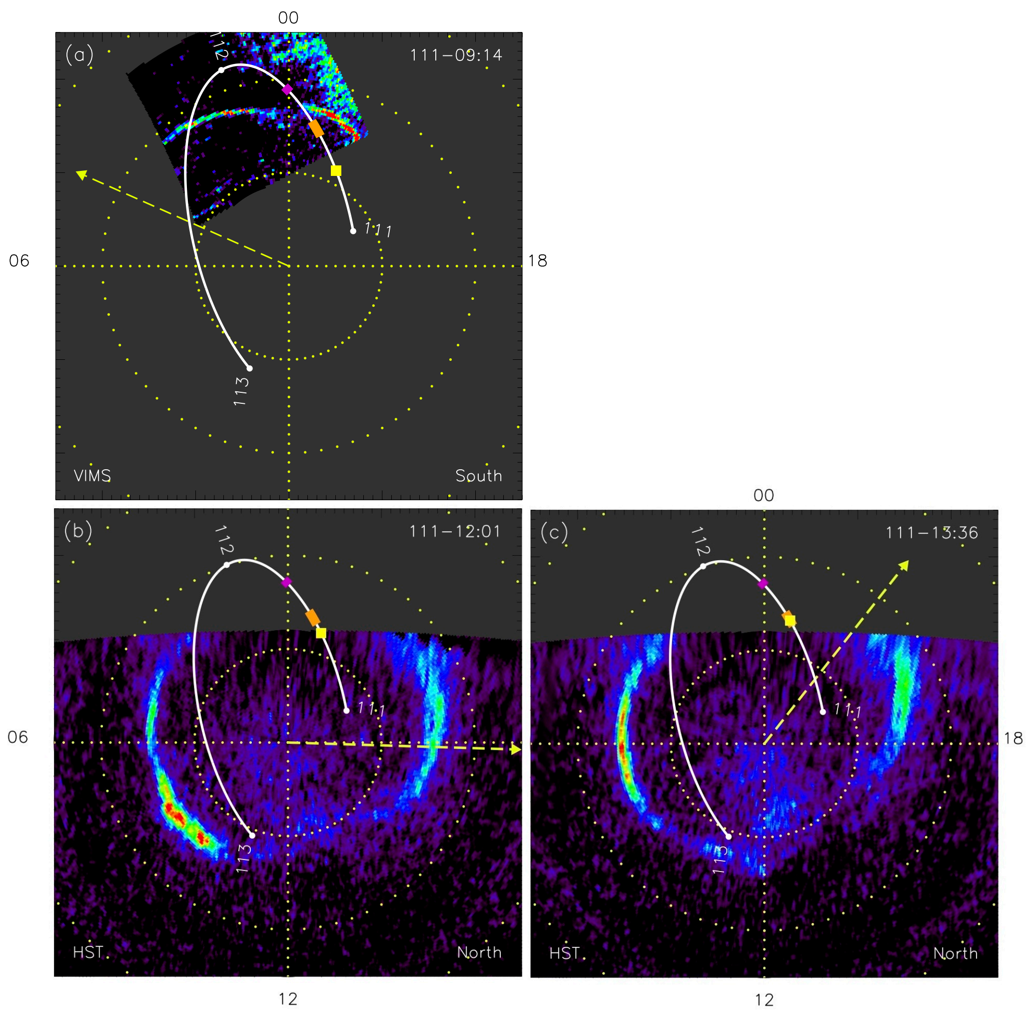

Figure 3: Observations of Saturn's aurorae on 2013-111. Local noon is to the bottom and dawn to the left. The yellow grid marks circles of latitude at intervals of 10° and the noon-midnight and dawn-dusk meridians. The white line shows the ionospheric footprint of Cassini's trajectory on 2013-111 to 2013-113 mapped into the appropriate ionosphere. The yellow square on this line indicates the position of Cassini at the time this image was taken, while the purple and orange shaded regions show the location of the upward and downward field-aligned current regions, respectively, determined from the magnetic field data in this hemisphere. The yellow dashed arrow indicates the direction in which the auroral oval is expected to be tilted at the time of the image. The hemisphere imaged and instrument used are labelled in the bottom of each panel.

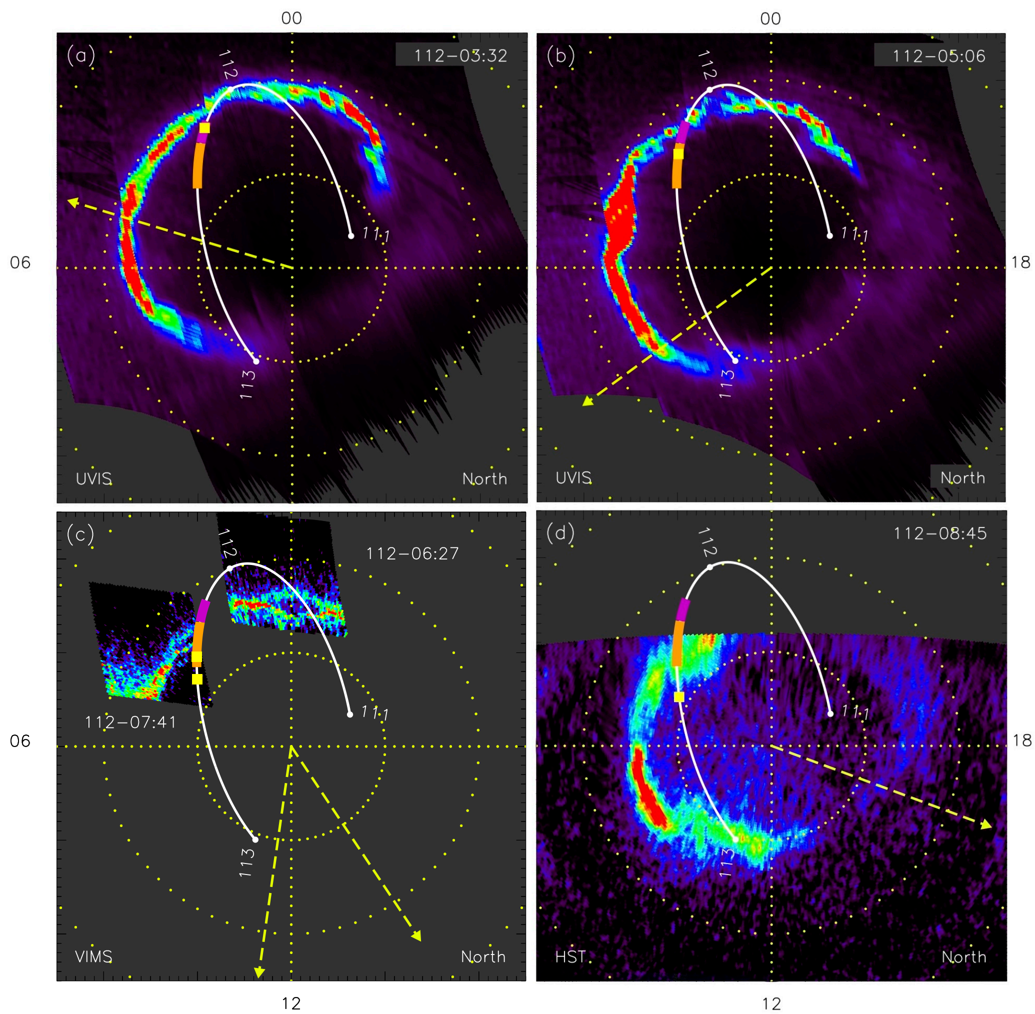

Figure 4: Observations of Saturn's aurorae on 2013-112 in the same format as Figure 3.

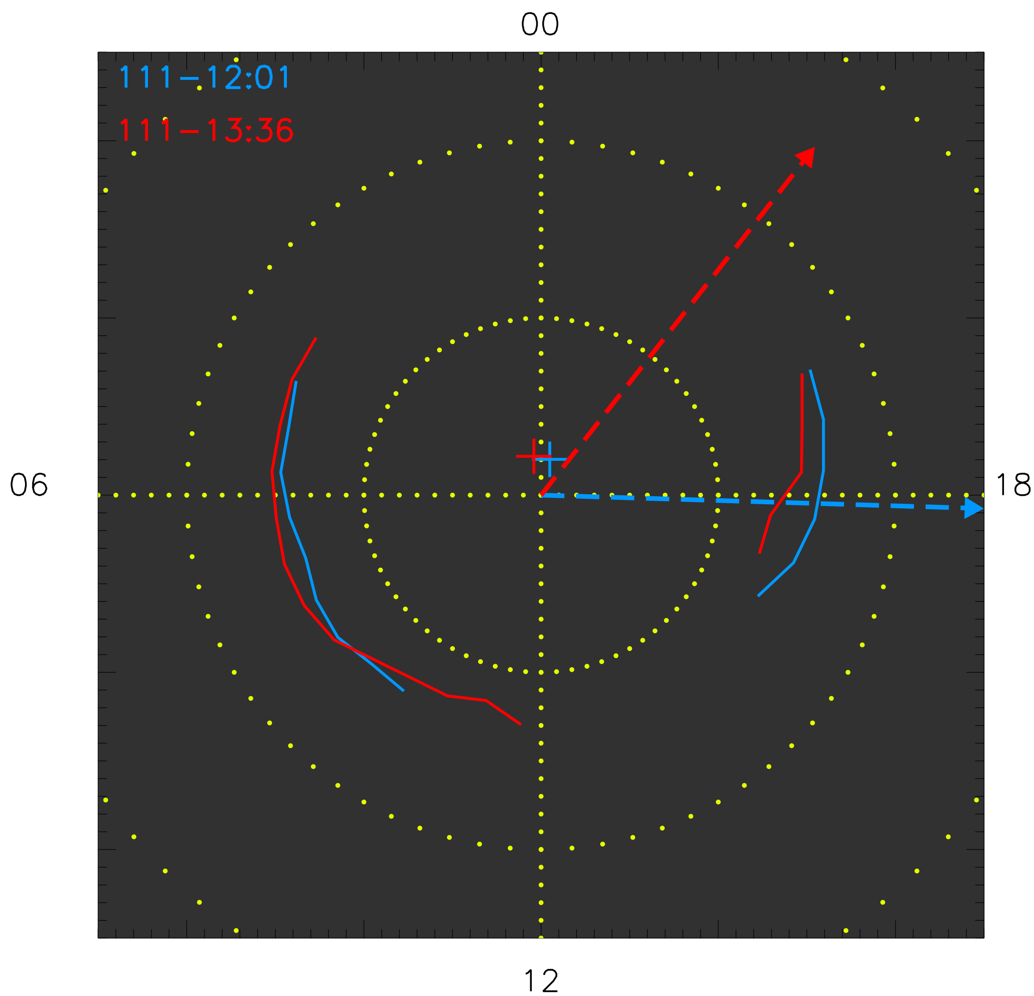

Figure 5: Location of the peak northern auroral emission on 2013-111 in the same orientation as Figure 3. The crosses indicate the centre of a best fit circle in each case. The dashed arrow indicates the direction in which the northern auroral oval is expected to be tilted at the centre time of each image.

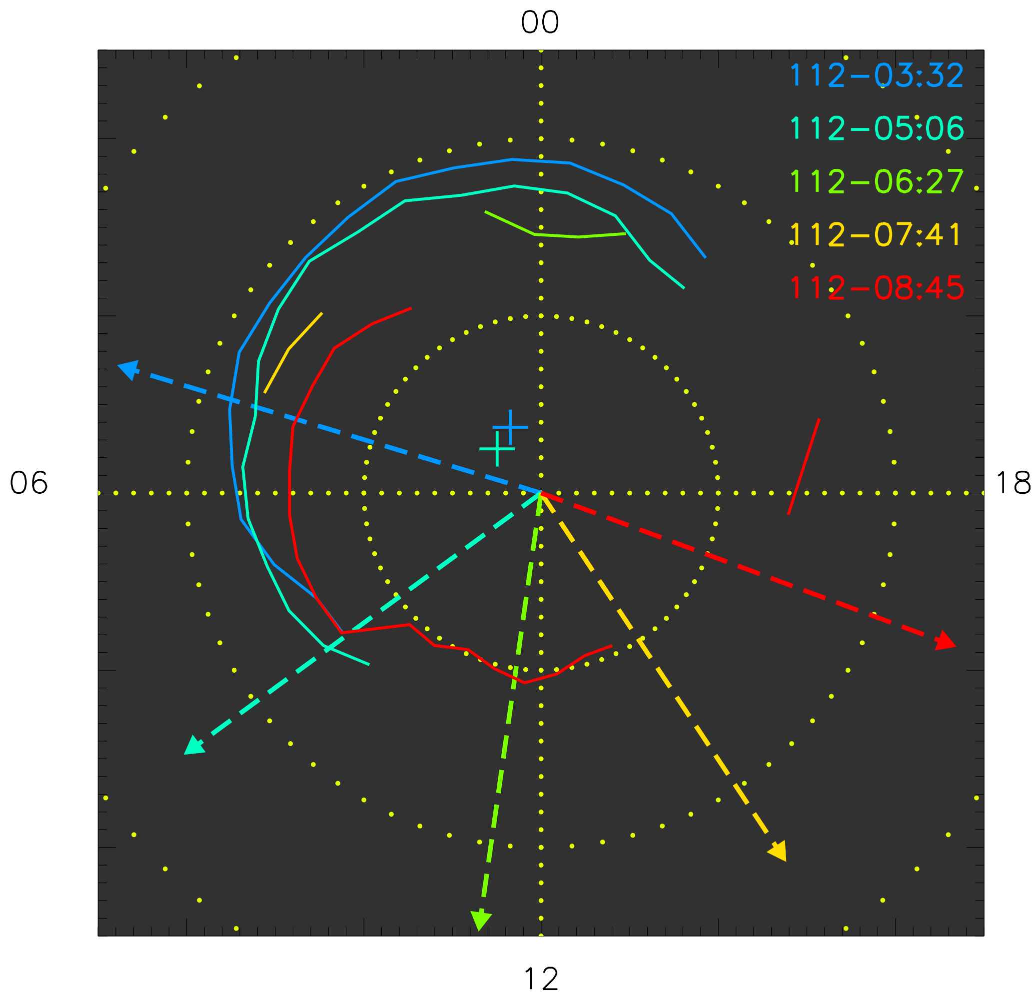

Figure 6: As Figure 5 but for auroral observations on 2013-112.